

Suppression of the elastic scattering cross section for $^{17}\text{Ne} + ^{208}\text{Pb}$ system

Kyoungsu Heo and Myung-Ki Cheoun

*Department of Physics and Origin of Matter and Evolution of Galaxies (OMEG) Institute,
Soongsil University, Seoul 06978, Korea*

Ki-Seok Choi and K. S. Kim

School of Liberal Arts and Science, Korea Aerospace University, Koyang 10540, Korea

W. Y. So*

*Department of Radiological Science, Kangwon
National University at Dogye, Samcheok 25945, Korea*

(Dated: September 19, 2023)

We investigated the elastic scattering, inelastic scattering, breakup reaction, and total fusion reactions of $^{17}\text{Ne} + ^{208}\text{Pb}$ system using the optical model (OM) and a coupled channel (CC) approaches. The aim of this study is to elucidate the suppress of the elastic cross-section that is invisible in proton-rich nuclei such as ^8B and ^{17}F projectiles but appears in neutron-rich nuclei such as ^{11}Li and ^{11}Be projectiles. The results revealed that this suppression was caused mainly by the nuclear interaction between the projectile and target nucleus rather than the strong Coulomb interaction observed in neutron-rich nuclei and the contributions of Coulomb excitation interaction due to two low-lying E2 resonance states are relatively small. From the simultaneous χ^2 analysis of the $^{17}\text{Ne} + ^{208}\text{Pb}$ system, we can infer a strong suppression effect in the elastic scattering cross-section due to the nuclear interaction between the projectile and target nucleus, rather than the Coulomb interaction as observed in neutron-rich nuclei. Also, the contribution of the direct reaction, comprising the inelastic scattering and breakup reaction cross-sections, accounted for almost half of the total reaction. Finally, we perform the CC calculation using the parameters obtained from our OM calculation but our CC calculations could not explain the ^{15}O production cross section.

I. INTRODUCTION

Due to the recent development of the rare isotope (RI) technology, neutron- or proton-rich nuclei can be used as projectiles to collide with heavy target nuclei such as ${}^6\text{He} + {}^{208}\text{Pb}$ [1, 2], ${}^{11}\text{Li} + {}^{208}\text{Pb}$ [3], ${}^{11}\text{Be} + {}^{197}\text{Au}$ [4], ${}^8\text{B} + {}^{\text{Nat}}\text{Pb}$ [5], and ${}^{17}\text{F} + {}^{208}\text{Pb}$ [6–8] systems. A characteristic of these projectiles is their weakly bound, which is reflected by the low separation energies. Specifically, the separation energies of ${}^6\text{He}$ ($S_{2n} = 0.975$ MeV [1]), ${}^{11}\text{Li}$ ($S_{2n} = 0.369$ MeV [3]), ${}^{11}\text{Be}$ ($S_n = 0.503$ MeV [9]), ${}^8\text{B}$ ($S_p = 0.138$ MeV [5]), and ${}^{17}\text{F}$ ($S_p = 0.601$ MeV [6]) are less than 1 MeV, considerably smaller than those of the well-known strongly bound ${}^{12}\text{C}$ ($S_p = 15.956$ MeV [10]) and ${}^{16}\text{O}$ ($S_p = 12.127$ MeV [10]) nuclei.

This implies that the projectile can be facily separated into the core nuclei and valence nucleon(s) by the Coulomb interaction and/or the nuclear interaction with the target nuclei. Consequently, the flux toward the elastic scattering channel is strongly diminished because of this strong breakup effect. This phenomenon is particularly prominent in ${}^{11}\text{Li}$ and ${}^{11}\text{Be}$ projectiles with valence neutron(s), as depicted in Fig. 3 of Ref. [3] and Fig. 1 of Ref. [11]. However, in case of ${}^8\text{B}$ and ${}^{17}\text{F}$ projectiles with a valence proton, this phenomenon is not observed clearly. Indeed, as shown in Fig. 6 of Ref. [5], the quasielastic scattering data of ${}^8\text{B} + {}^{\text{Nat}}\text{Pb}$ system were very similar to those of ${}^7\text{Be} + {}^{\text{Nat}}\text{Pb}$ system at $E_{\text{lab}}/V_B \approx 3$. Here E_{lab}/V_B denotes the ratio of between the incident beam energy (E_{lab}) and the Coulomb barrier energy (V_B). This signifies that the breakup effect on elastic scattering is not substantially large in the nuclear reaction of the proton-rich nuclei, as reported in Ref. [5].

These facts raise the question of why the suppression of the elastic scattering cross-sections fails to occur in the collision process between the heavy targets and proton-rich projectiles such as ${}^8\text{B}$ and ${}^{17}\text{F}$ nuclei. One hypothesis to interpret this question is the shielding effect [12, 13]. Fundamentally, the valence proton in ${}^8\text{B}$ and ${}^{17}\text{F}$ projectiles is repelled by the target nuclei. However, unlike valence neutrons, in the case of valence protons, they are strongly pushed back by the Coulomb repulsion from the target nucleus, causing them to effectively hide behind the heavier core nucleus. This results in a shielding effect where the influence from the target nucleus is diminished. Consequently, the breakup

*e-mail: wyso@kangwon.ac.kr

reaction cross-sections do not constitute a large proportion, as listed in Table II of Ref. [14]. This is in contrast to the phenomenon observed in ^{11}Li and ^{11}Be projectiles, which lack this shielding effect due to the presence of valence neutrons [15].

Recently, the elastic scattering data of $^{17}\text{Ne} + ^{208}\text{Pb}$ system were reported at energy proximate to the Coulomb barrier [16]. According to Ref. [16], the suppression effect in elastic scattering cross-sections has been reported in nuclear reactions with the proton-rich nucleus. In principle, ^{17}Ne is one of the proton-rich nuclei with the Borromean structure interconnected by the three nucleus, $^{15}\text{O} + \text{p} + \text{p}$ [16, 17]. In contrast to ^8B and ^{17}F nuclei, it can be inferred that the inelastic and/or breakup reactions significantly contributed toward the total reaction at energy proximate to the Coulomb barrier. This differs from the characteristics of nuclear reactions involving the proton-rich nuclei reported thus far. Therefore, this study aims to examine the cause of the suppression in elastic scattering cross-sections of the proton-rich projectile ^{17}Ne and ^{208}Pb target nuclei system.

In the Ref. [16], they analyzed elastic scattering data for the $^{17}\text{Ne} + ^{208}\text{Pb}$ system using OM and CC methods similar to our approach. However, their OM method involved fitting only the elastic scattering data except for the breakup cross section by employing a single real volume part and a pair of imaginary volume + surface parts. As a result, while their outcomes could describe the elastic scattering data well, the calculation of the breakup cross section was not achieved and could not be reproduced. For reference, we will consider the ^{15}O production cross section as the breakup cross section in our calculations. In addition, they attempted to reproduce the elastic scattering and breakup cross section by performing CC calculations to use the $\frac{3}{2}^-$ with $E_x = 1.288$ MeV and $\frac{5}{2}^-$ with $E_x = 1.764$ MeV resonance states. Unfortunately, their approach focused on reproducing elastic scattering data. As a result, they could achieve a good description of the elastic scattering but could not explain the experimental data of the breakup cross section.

In our present work, hence, we aim to explain simultaneously the elastic scattering and breakup cross section data using both the OM and CC methods different from Ref. [16]. In particular, in the OM method, channels to be considered will be separated through available experimental data. Using the separated channels, then, we will calculate the elastic scattering, inelastic scattering, breakup reaction, and fusion cross sections, which were not shown in Ref. [16], and examine the contribution of these channels. Furthermore, in the CC calculations, the elastic scattering and breakup cross section data are explained considering

the new $\frac{5}{2}^-$ state with $E_x = 2.692$ MeV as well as the $\frac{3}{2}^-$ and $\frac{5}{2}^-$ resonance states mentioned in Ref. [16].

The remainder of this paper is organized as follows. In Sec. II, we explain the formalism for the optical model (OM) used in this study. Based on all available experimental data, we evaluate the various cross-sections related to the elastic scattering, inelastic scattering, breakup reaction, and fusion reaction from the OM. Additionally, in Sec. III, we introduce dynamic polarization potentials (DPPs) to explain the reaction channels. Thereafter, we discuss the characteristics of proton-rich projectile, ^{17}Ne , obtained from this study. Ultimately, the conclusions of this research are summarized in Sec. IV.

II. FORMALISM

To investigate the suppression of the experimental P_{el} values for $^{17}\text{Ne} + ^{208}\text{Pb}$ system, we employ the OM method with the Schrödinger equation as follows [19–21]:

$$[E - T_l(r)]\chi_l^{(+)}(r) = U_{\text{OM}}(r) \chi_l^{(+)}(r) \quad (1)$$

where $T_l(r)$ and $\chi_l^{(+)}(r)$ represent a kinetic energy operator and a distorted partial wave function expressed as a function of the angular momentum l , respectively. The OM potential $U_{\text{OM}}(r)$ in Eq. (1) is composed of the real monopole Coulomb potential $V_{\text{C}}(r)$, the energy independent real bare potential $V_0(r)$, and the energy dependent complex dynamic polarization potential (DPP) $U_{\text{DPP}}(r)$ as follows [14]:

$$\begin{aligned} U_{\text{OM}}(r) &= V_{\text{C}}(r) - V_0(r) - U_{\text{DPP}}(r) \\ &= V_{\text{C}}(r) - V_0(r) - U_{\text{DR}}(r) - U_{\text{F}}(r) \\ &= V_{\text{C}}(r) - V_0(r) - U_{\text{inel}}(r) - U_{\text{br}}(r) - U_{\text{F}}(r) \\ &= V_{\text{C}}(r) - V_0(r) - iW_{\text{inel}}^{\text{C}}(r) - U_{\text{inel}}^{\text{N}}(r) - iW_{\text{br}}^{\text{C}}(r) - U_{\text{br}}^{\text{N}}(r) - U_{\text{F}}(r). \end{aligned} \quad (2)$$

In Eq. (2), $V_0(r)$ denotes the real bare potential with a volume-type Woods-Saxon potential that is an independent potential for the incident energy of the projectile, expressed as

$$V_0(r) = V_0 \left[1 + \exp\left(\frac{r - R_0}{a_0}\right) \right]^{-1} \quad (3)$$

with $R_0 = r_0 (A_1^{1/3} + A_2^{1/3})$. A_1 and A_2 represent the mass numbers for the projectile and target nuclei. For reference, this real bare potential is actually created by reconstituting the

São Paulo potential (SPP) as follows [22]: we first construct the SPP (the dashed red line) using the nuclear densities for both ^{17}Ne and ^{208}Pb nucleus as shown in Fig. 1. As shown in Fig. 1, however, the SPP based on the folding potential has a very deep depth parameter. To solve this problem, thus, we newly parameterize the SPP potential into the Woods-Saxon form utilizing the χ^2 -fitting which is performed to match well at $r \geq 11$ fm, where a strong absorption reaction occurs. As a result, we are able to obtain a new Woods-Saxon type potential (bare potential) denoted as the solid black line in Fig. 1. At near barrier incident energy region, when the projectile and the target nucleus come close together, the nuclear reaction at the surface becomes very important because the two nuclei cannot collide very deeply. For this reason, we consider the χ^2 -fitting more precisely to the outside rather than the inside of the potential. In order to compare the newly obtained bare potential with ones provided by Akyuz-Winther (AW) [23] and Ref. [16] (the dotted blue and dash-dotted green lines), in addition, these potentials are drawn together in Fig. 1, and each potential parameter is listed in Table I. One interesting point is that our bare potential and the AW potential are similar, as shown in Fig. 1 and Table I.

TABLE I: Parameter sets of the bare potentials for $^{17}\text{Ne} + ^{208}\text{Pb}$ system.

Model	V_0 (MeV)	a_0 (fm)	r_0 (fm)
Bare (present)	67.0	0.692	1.196
AW [23]	70.6	0.660	1.178
Ref. [16]	63.5	0.309	1.300

According to the incident energy of the projectile, the DPP denoted as $U_{\text{DPP}}(r)$ can be segmented into the DR and fusion reaction potentials. In the DR channels, several channels exist such as the inelastic scattering, breakup reaction, transfer reaction, and so on. In this research, we divide the DR channels into the inelastic scattering channel and remaining channels composed of the breakup reaction channel, transfer reaction channel, etc. More specifically, we expressed the potentials related to these channels as $U_{\text{inel}}(r)$ and $U_{\text{br}}(r)$, respectively, in Eq. (2).

Considering Refs. [16–18], the ^{17}Ne has no excited state below two proton separation

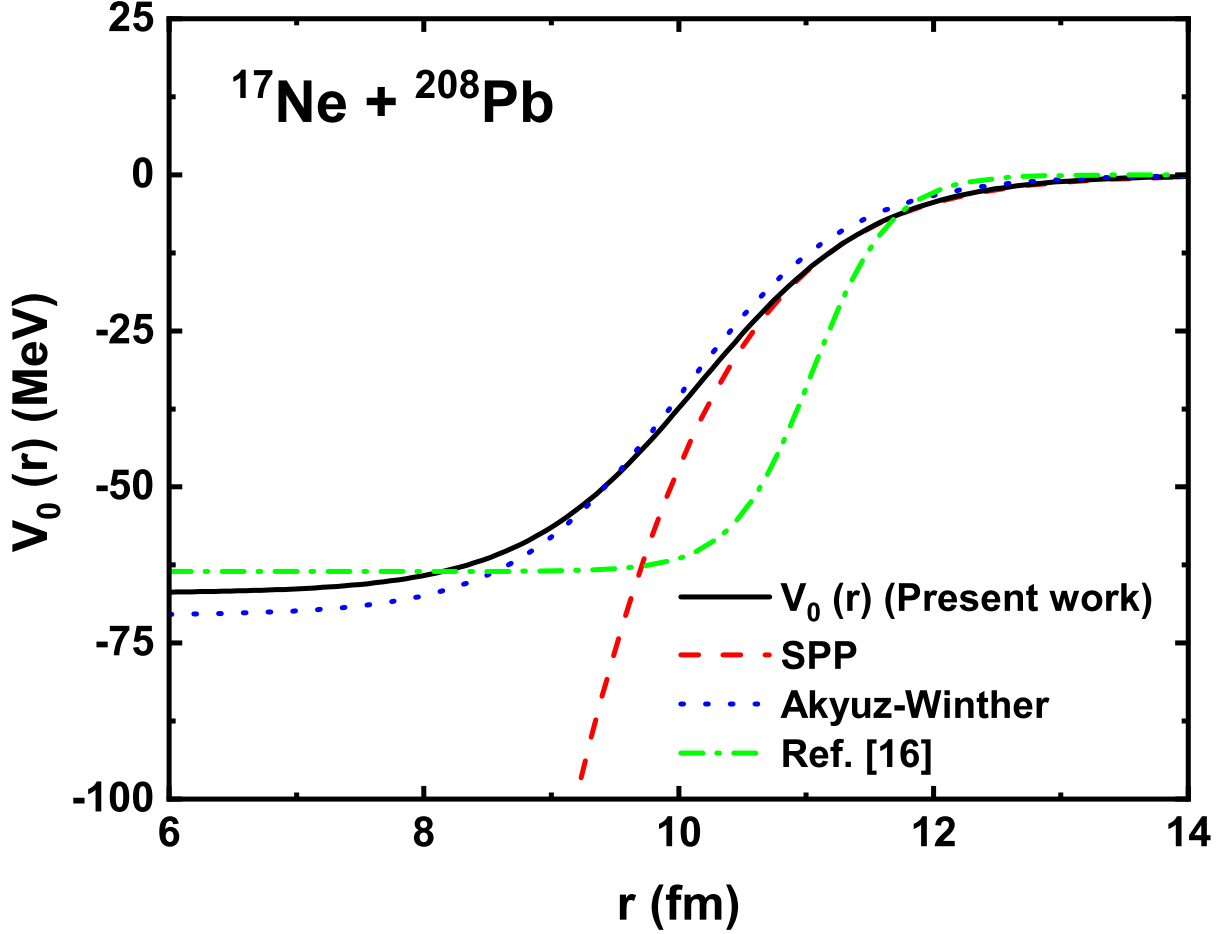


FIG. 1: The bare potentials for $^{17}\text{Ne} + ^{208}\text{Pb}$ system. The dashed red line shows the SPP made using nuclear densities for both ^{17}Ne and ^{208}Pb nucleus. The solid black line represent a newly parameterized the SPP potential with the Woods-Saxon type utilizing the χ^2 -fitting. The dotted blue and dash-dotted green lines represent the potentials provided by Akyuz-Winther [23] and Ref. [16].

energy ($S_{2p} = 0.944$ MeV). Instead, there are three low-lying resonance states, which are $\frac{3}{2}^-$ state [$E_x = 1.288$ MeV and $B(E2) = 95_{-36}^{+26}e^2\text{fm}^4$ or $66_{-25}^{+18}e^2\text{fm}^4$], $\frac{5}{2}^-$ state [$E_x = 1.764$ MeV and $B(E2) = 90 \pm 18e^2\text{fm}^4$ or $179 \pm 26e^2\text{fm}^4$], and $\frac{3}{2}^-$ state [$E_x = 2.692$ MeV and $B(E2) = 69 \pm 10e^2\text{fm}^4$], above two proton separation energy. Here E_x is an excitation energy. In the $\frac{3}{2}^-$ [$E_x = 1.288$ MeV] state, it is possible two decay mode by either concurrent $2p$ emission or gamma ray emission. Since the probability of simultaneous $2p$ emission are less than 0.77%, however, it is reported that mostly only gamma emission are observed. In our present work, as a result, the channel due to the coupling between this excited state ($\frac{3}{2}^-$) and ground state

($\frac{1}{2}^-$) will be regarded as an inelastic scattering channel. On the other hand, in the case of $\frac{5}{2}^-$ state, it was reported in Ref. [17] that no evidence for the gamma emission and simultaneous $2p$ emission could be measured experimentally. Instead, it has a decay mode in which ^{17}Ne projectile is changed to ^{15}O nucleus through two sequential proton emission. In the case of $\frac{3}{2}^-$ state with $E_x = 2.692$ MeV, also, it has the two sequential proton emission mode as with the case of $\frac{5}{2}^-$ state. As a result, these two channels ($\frac{5}{2}^-$ state with $E_x = 1.764$ MeV and $\frac{3}{2}^-$ state with $E_x = 2.692$ MeV) are associated with the inclusive ^{15}O angular distribution and will be regarded as a breakup channel not an inelastic scattering one in this work.

To consider the Coulomb excitation effect for inelastic scattering and/or breakup channel, we introduced the Coulomb excitation potential. This involves various interactions such as the Coulomb dipole excitation (CDE; E1 transition), Coulomb quadrupole excitation (CQE; E2 transition), and so forth. As mentioned above, however, in the case of the inelastic scattering and/or breakup channel for ^{17}Ne projectile, since it is related to the E2 transition, we only need to consider the CQE interaction with an imaginary potential, described as follows [24]:

$$W_{\text{inel. (br)}}^{\text{C}}(r) = \begin{cases} -\left[1 - \frac{2}{7}\left(\frac{r_C}{r}\right)^2 - \frac{1}{21}\left(\frac{r_C}{r}\right)^4\right] \left[1 - \left(\frac{Z_1 Z_2 e^2}{r E_{c.m.}}\right)\right]^{-1/2} \frac{W_P}{r^5} & \text{for } r \geq r_C \\ -\frac{2\sqrt{10}}{3} \frac{W_P r^4}{r_C^9} & \text{for } r < r_C \end{cases} \quad (4)$$

with

$$W_P = 0.01676 \frac{\mu Z_2^2}{k} B(E2) g_2(\xi). \quad (5)$$

Here, $B(E2)$ represent the quadrupole electric transition strength related to the E2 transition and $g_2(\xi)$ indicate an adiabaticity correction factor given as a function of the adiabaticity parameter $\xi = a_0 \varepsilon / \hbar v$ [14, 24, 25]. Z_2 denotes the charge number of the target nucleus.

To investigate the breakup effect of the $^{17}\text{Ne} + ^{208}\text{Pb}$ system, we have to consider the remaining DR channels excluding the inelastic scattering channels. Similar to the inelastic scattering mentioned earlier, the breakup effect can be classified into a nuclear interaction component and a Coulomb excitation component, because it mainly occurs on the surface or at the long region distance caused by the Coulomb and nuclear forces acting between the projectile and target nucleus. In order to consider the breakup effect by the Coulomb interaction, as mentioned above, the CQE potential in Eq. (4) can be used as it is. To explain the breakup effect occurring near the nucleus surface via nuclear interaction, next,

we manipulated the nuclear interaction component of $U_{\text{br}}(r)$ potential as another Wood-Saxon potential with the surface-type constituent as follows [26]:

$$U_{\text{br}}^{\text{N}}(r) = -4 a_{\text{i, br}}^{\text{N}} (V_{\text{br}}^{\text{N}} + iW_{\text{br}}^{\text{N}}) \frac{d[1 + \exp(X_{\text{i, br}}^{\text{N}})]^{-1}}{dr}, \quad \text{i} = V \text{ and } W, \quad (6)$$

where $X_{\text{i, br}}^{\text{N}} = (r - R_{\text{i, br}}^{\text{N}})/a_{\text{i, br}}^{\text{N}}$ with $R_{\text{i, br}}^{\text{N}} = r_{\text{i, br}}^{\text{N}} (A_1^{1/3} + A_2^{1/3})$. Note that the potential form used to explain the breakup reaction by the nuclear interaction is the same as the differential form of Woods-Saxon type used in the inelastic scattering by the nuclear one and that the meaning of the remaining DR except for the inelastic channel “br” is formed by the breakup reaction channel, transfer reaction channel, etc.

Ultimately, the fusion reaction of the DPP primarily occurred not on the nucleus surface, but rather deep inside. Therefore, the fusion potential will be considered as a volume-type Woods-Saxon potential herein as follows:

$$U_{\text{F}}(r) = (V_{\text{F}} + iW_{\text{F}}) [1 + \exp(X_{\text{i, F}})]^{-1}, \quad \text{i} = V \text{ and } W, \quad (7)$$

where $X_{\text{i, F}} = (r - R_{\text{i, F}})/a_{\text{i, F}}$ with $R_{\text{i, F}} = r_{\text{i, F}} (A_1^{1/3} + A_2^{1/3})$. Note that the meaning of fusion “F” is formed by the total fusion combining the complete and incomplete fusion in this research.

III. RESULTS

A. OM calculations

As depicted in the dotted magenta line of Fig. 2 (a), the experimental P_{el} ratio of $^{17}\text{Ne} + ^{208}\text{Pb}$ system cannot be reproduced through a potential defined as the sum of $V_0(r)$ and $U_{\text{F}}(r)$ in Eq. (2). This signifies that the additional absorption channels are open near Coulomb barrier energy region. Therefore, the additional DPPs should be inferred to reproduce the experimental results. This study considered the inelastic scattering, breakup reaction, and fusion reaction as the additional DPPs.

In principle, to explain the elastic scattering data for $^{17}\text{Ne} + ^{208}\text{Pb}$ system using these DPPs, various experimental data are required as the input data. In $^{17}\text{Ne} + ^{208}\text{Pb}$ system, however, there exist two experimental data including the elastic scattering and breakup cross-section data. Nevertheless, we can calculate the total fusion cross-sections between incident isotopes and target nucleus through one channel calculation using CCFULL code [27].

The extracted total fusion cross section obtained from the barrier penetration model (BPM) using $V_0(r)$ in Eq. (2) is about 994.3mb.

Utilizing the experimental elastic scattering, the experimental breakup reaction, and the theoretical total fusion cross-section data, we performed the χ^2 analysis. As discussed earlier, the breakup reactions occur primarily near the surface of the projectile and target nucleus; therefore, we employed the differential form of Woods-Saxon potential in the calculations presented in Eq. (6). Consequently, the χ^2 fitting could be performed on twelve adjustable parameters ($V_{\text{br}}^{\text{N}}, W_{\text{br}}^{\text{N}}, a_{\text{v, br}}^{\text{N}}, a_{\text{w, br}}^{\text{N}}, r_{\text{v, br}}^{\text{N}}, r_{\text{w, br}}^{\text{N}}, V_{\text{F}}, W_{\text{F}}, a_{\text{v, F}}, a_{\text{w, F}}, r_{\text{v, F}}, r_{\text{w, F}}$) in $U_{\text{br}}^{\text{N}}(r)$ and $U_{\text{F}}(r)$. However, as certain adjustable parameters were entangled, we reduced the parameters in this χ^2 fitting by applying it on eight adjustable parameters ($V_{\text{br}}^{\text{N}}, W_{\text{br}}^{\text{N}}, a_{\text{br}}^{\text{N}}, r_{\text{br}}^{\text{N}}, V_{\text{F}}, W_{\text{F}}, a_{\text{F}}, r_{\text{F}}$) by assuming the diffuseness and radius parameters as $a_{\text{v, br}}^{\text{N}} = a_{\text{w, br}}^{\text{N}} \equiv a_{\text{br}}^{\text{N}}, a_{\text{v, F}} = a_{\text{w, F}} \equiv a_{\text{F}}, r_{\text{v, br}}^{\text{N}} = r_{\text{w, br}}^{\text{N}} \equiv r_{\text{br}}^{\text{N}}$, and $r_{\text{v, F}} = r_{\text{w, F}} \equiv r_{\text{F}}$.

The parameters obtained from χ^2 fitting are listed in set (A) of Table II. Based on these parameters, we plotted the theoretical P_{el} ratio (The ratio of the elastic scattering cross section and the Rutherford cross section) and the angular distribution of the breakup cross-section as the dashed blue line in Fig. 2. Overall, the theoretical P_{el} ratio and the angular distribution of the breakup cross-section are consistent with the experimental ratio except for one or two points as shown in Fig. 2. One interesting point is that the rainbow peak seen around $\theta_{\text{c.m.}} = 60^\circ$ in the dotted magenta line is strongly suppressed due to the effect of inelastic scattering and the breakup reactions. This was considered to be caused by the characteristic of ^{17}Ne nucleus with relatively low the excited energy ($E_x^{1st} = 1.288\text{MeV}$) and the separation energy ($S_p = 1.464\text{ MeV}$) such as weakly bound ^{11}Li and ^{11}Be nuclei.

To investigate angular distribution of the breakup cross-section, for reference, we use the following form [20]:

$$\frac{d\sigma_{\text{br}}}{d\Omega} = \frac{ka_0}{16\pi} \frac{1}{\cos(\frac{\theta_{\text{c.m.}}}{2}) \sin^3(\frac{\theta_{\text{c.m.}}}{2})} \sum_l \frac{\pi}{k} (2l+1) T_{\text{br};l}, \quad (8)$$

with

$$T_{\text{br};l} = \frac{8}{\hbar v} \int_0^\infty |\chi_l^+(r)|^2 [W_{\text{br}}(r)] dr = \frac{8}{\hbar v} \int_0^\infty |\chi_l^+(r)|^2 [W_{\text{br}}^{\text{N}}(r) + W_{\text{br}}^{\text{C}}(r)] dr. \quad (9)$$

Furthermore, we evaluated the inelastic, breakup, and fusion cross-sections ($\sigma_{\text{inel.}}, \sigma_{\text{br.}}$, and σ_{F}) expressed as [28, 29]

$$\sigma_i = \frac{2}{\hbar v} \langle \chi^+(r) | W_i(r) | \chi^+(r) \rangle \quad i = \text{inel.}, \text{br.}, \text{and F.} \quad (10)$$

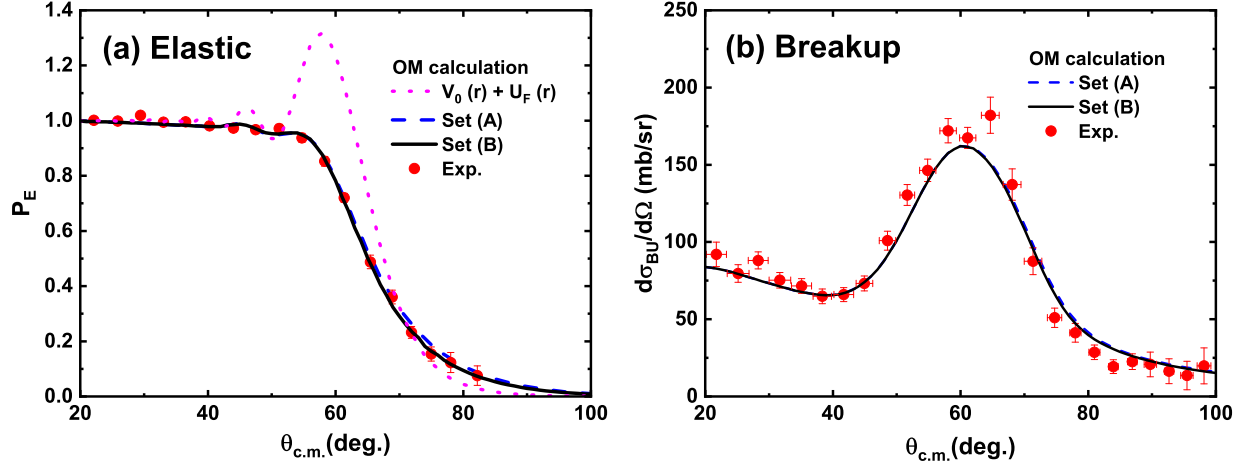


FIG. 2: (a) P_{el} ratios and (b) angular distributions of breakup (^{15}O production) cross-section for $^{17}\text{Ne} + ^{208}\text{Pb}$ system. The dashed blue and solid black lines denote the theoretical ratios P_{el} and angular distributions using the parameter sets (A) and (B) in Table II, respectively. The solid red circles denote the experimental data taken from Ref. [16] for $^{17}\text{Ne} + ^{208}\text{Pb}$ system at $E_{lab} = 136$ MeV. Note that the dotted magenta line indicates P_{el} ratio only based on the $V_0 + U_F$ in Eq. (2). Additionally, U_F has been extracted through the set(B). In order to perform these calculations, for reference, we used the $\frac{3}{2}^-$ state [$E_x = 1.288$ MeV and $B(E2) = 41$ e $^2\text{fm}^4$] for the inelastic interaction, and the $\frac{5}{2}^-$ state [$E_x = 1.764$ MeV and $B(E2) = 72$ e $^2\text{fm}^4$] and $\frac{3}{2}^-$ state [$E_x = 2.692$ MeV and $B(E2) = 59$ e $^2\text{fm}^4$] for the breakup one. Note that these values correspond to the minimum value of $B(E2)$ introduced in Refs. [16–18].

TABLE II: Optimized parameter sets of DPPs for $^{17}\text{Ne} + ^{208}\text{Pb}$ system.

Set	Inelastic scattering				Breakup				Fusion				χ^2
	V_{inel}^N	W_{inel}^N	a_{inel}^N	r_{inel}^N	V_{br}^N	W_{br}^N	a_{br}^N	r_{br}^N	V_F	W_F	a_F	r_F	
	(MeV)	(MeV)	(fm)	(fm)	(MeV)	(MeV)	(fm)	(fm)	(MeV)	(MeV)	(fm)	(fm)	
(A)	–	–	–	–	0.354	0.142	0.760	1.627	-5.164	7.305	0.222	1.44	2.6
(B)	-2.826	1.305	0.178	1.451	0.354	0.142	0.760	1.627	46.088	94.720	0.340	1.28	2.1

These values are listed in set (A) of Table III. Notably, we used $W_i(r)$ in Eq. (10) as $W_{inel.}(r) = W_{inel.}^N(r) + W_{inel.}^C(r)$, $W_{br}(r) = W_{br}^N(r) + W_{br}^C(r)$, and $W_F(r)$ for $\sigma_{inel.}$, σ_{br} , and σ_F , respectively.

TABLE III: Inelastic scattering, breakup, total fusion, and total reaction cross sections for $^{17}\text{Ne} + ^{208}\text{Pb}$ system at $E_{\text{lab}} = 136$ MeV. Set (A) and set (B) are the results by the sets in Table II.

	set	$\sigma_{\text{inel.}}$		σ_{br}		σ_{F}	σ_{R}
		$\sigma_{\text{inel}}^{\text{N}}$	$\sigma_{\text{inel}}^{\text{C}}$	$\sigma_{\text{br}}^{\text{N}}$	$\sigma_{\text{br}}^{\text{C}}$		
		(mb)	(mb)	(mb)	(mb)		
Present work (OM)	(A)	–	130.4	320.0	282.7	1126.8	1859.9
Present work (OM)	(B)	250.9	128.3	316.4	278.1	915.6	1889.3
Ref. [16] (OM)		–	–	–	–	–	1800.0
Ref. [16] (CC)			350.0	–	–	–	1903.0

Based on the calculations performed thus far, we determined the contribution of the elastic scattering, inelastic scattering, breakup, and total fusion cross-sections of $^{17}\text{Ne} + ^{208}\text{Pb}$ system as shown in set (A) of Table III. Owing to the absence of the experimental inelastic scattering cross-section data, however, the contribution of each part (nuclear and Coulomb) for inelastic scattering cross-section could not be adequately investigated. Since inelastic scattering channel can also be caused by the nuclear interaction as well as Coulomb one, as is well known, we must also consider the inelastic scattering channel by the nuclear interaction. In particular, the absence of the nuclear part of inelastic scattering interaction can be a possibility that the flux corresponding to this interaction has flowed into other reaction channels. In fact, as shown in set (A) of Table III, it can be seen that the total fusion cross section obtained in our calculation (1126.8mb) is about 132.5mb larger than that obtained in CC one (994.3mb). In order to isolate the nuclear part of inelastic scattering interaction, thus, we will hire a new interaction. As the inelastic scattering primarily occurred near the nucleus surface, in general, the nuclear component of the inelastic scattering potential was considered with a differential form of the Woods-Saxon potential, expressed as follows [26]:

$$U_{\text{inel.}}^{\text{N}}(r) = -4 a_{\text{i,inel}}^{\text{N}} (V_{\text{inel}}^{\text{N}} + iW_{\text{inel}}^{\text{N}}) \frac{d[1 + \exp(X_{\text{i,inel}}^{\text{N}})]^{-1}}{dr}, \quad \text{i} = V \text{ and } W, \quad (11)$$

where $X_{\text{i,inel}}^{\text{N}} = (r - R_{\text{i,inel}}^{\text{N}})/a_{\text{i,inel}}^{\text{N}}$ with $R_{\text{i,inel}}^{\text{N}} = r_{\text{i,inel}}^{\text{N}} (A_1^{1/3} + A_2^{1/3})$.

With the differential form of the Woods-Saxon potential corresponding to the nuclear component of the inelastic scattering potential, as a result, we performed the additional χ^2 fitting using $U_{\text{DPP}}(r) = U_{\text{inel}}^{\text{N}}(r) + iW_{\text{inel}}^{\text{C}}(r) + U_{\text{br}}^{\text{N}}(r) + U_{\text{br}}^{\text{C}}(r) + U_{\text{F}}(r)$ in Eq. (2). For

reference, $W_{\text{inel}}^{\text{C}}(r)$ and $U_{\text{br}}^{\text{C}}(r)$ potentials related to the CQE transition did not require any adjustable parameters. In principle, we should perform χ^2 fitting on eighteen adjustable parameters ($V_{\text{inel}}^{\text{N}}, W_{\text{inel}}^{\text{N}}, a_{\text{v, inel}}^{\text{N}}, a_{\text{w, inel}}^{\text{N}}, r_{\text{v, inel}}^{\text{N}}, r_{\text{w, inel}}^{\text{N}}, V_{\text{br}}^{\text{N}}, W_{\text{br}}^{\text{N}}, a_{\text{v, br}}^{\text{N}}, a_{\text{w, br}}^{\text{N}}, r_{\text{v, br}}^{\text{N}}, r_{\text{w, br}}^{\text{N}}, V_{\text{F}}, W_{\text{F}}, a_{\text{v, F}}, a_{\text{w, F}}, r_{\text{v, F}}, r_{\text{w, F}}$) in $U_{\text{inel}}^{\text{N}}(r)$, $U_{\text{br}}^{\text{N}}(r)$, and $U_{\text{F}}(r)$. Since we have already found the parameters related to the breakup reaction potential that reproduce the experimental breakup cross-section data well, nonetheless, we can fix them ($V_{\text{br}}^{\text{N}}, W_{\text{br}}^{\text{N}}, a_{\text{br}}^{\text{N}}, r_{\text{br}}^{\text{N}}$) obtained through the set (A) of Table II. To reduce the parameters, also, we assume the diffuseness and radius parameters of the inelastic scattering and total fusion potential as $a_{\text{v, inel}}^{\text{N}} = a_{\text{w, inel}}^{\text{N}} \equiv a_{\text{inel}}^{\text{N}}, r_{\text{v, inel}}^{\text{N}} = r_{\text{w, inel}}^{\text{N}} \equiv r_{\text{inel}}^{\text{N}}, a_{\text{v, F}} = a_{\text{w, F}} \equiv a_{\text{F}}$, and $r_{\text{v, F}} = r_{\text{w, F}} \equiv r_{\text{F}}$. the radius parameters. Thereafter, we perform to the second χ^2 fitting with eight adjustable parameters ($V_{\text{inel}}^{\text{N}}, W_{\text{inel}}^{\text{N}}, a_{\text{inel}}^{\text{N}}, r_{\text{inel}}^{\text{N}}, V_{\text{F}}^{\text{N}}, W_{\text{F}}^{\text{N}}, a_{\text{F}}^{\text{N}}, r_{\text{F}}^{\text{N}}$). The parameters obtained from χ^2 fitting are listed in the set (B) of Table II.

Based on the parameters in set (B) of Table II, we plotted the theoretical P_{el} ratio and angular distribution of the breakup cross-section emerging from the nuclear component for inelastic scattering interaction as the solid black line in Fig. 2. In these calculations, the theoretical P_{el} ratio and angular distribution of the breakup cross-section was consistent with the experimental data for almost all scattering angles except for one or two points. As can be seen from the set (B) of Table III, we can see that part of the fusion cross-section has shifted to inelastic scattering one due to the addition of a new nuclear part of the inelastic scattering interaction, as we expected.

Ultimately, we calculated the inelastic scattering, breakup reaction, and fusion cross-sections expressed in Eq. (10), which are listed in set (B) of Table III. As presented in set (B) of Table III, the inelastic scattering cross-sections exhibited a greater contribution through the nuclear interaction than by the Coulomb excitation one. In contrast, the breakup reaction cross-section can be seen that the contributions of the two interactions are similar. Another interesting point that the contribution of DR cross-section (the sum of the inelastic scattering and breakup reaction cross-sections) to the total reaction was approximately half ($\sigma_{\text{DR}}/\sigma_{\text{R}} \approx 0.52$) of the total reaction cross-section as shown in set (B) of Table III. This implied that a significant portion of the elastic scattering channel was converted to the DR channel, such as the inelastic scattering and breakup reaction.

According to Ref. [16], the authors remarked that the Coulomb excitation interaction due to two low-lying E2 resonance states is not the main contribution to the imaginary part of

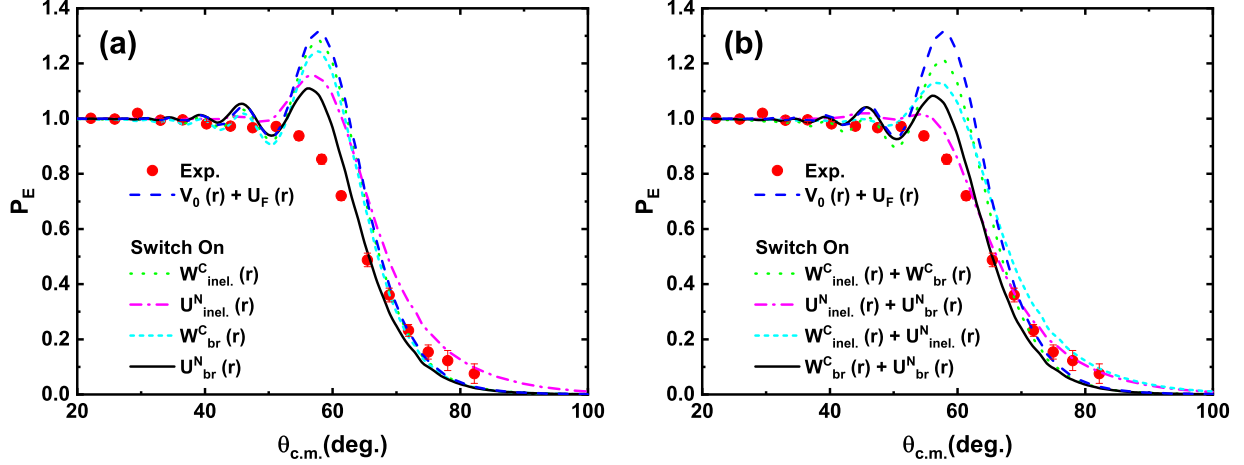


FIG. 3: Same as Fig. 2 but for the contribution of each channel. P_{el} ratios obtained from the (a) single channel and (b) two channel coupling for $^{17}\text{Ne} + ^{208}\text{Pb}$ system. The dashed blue lines denote the theoretical P_{el} ratios obtained from $V_0(r) + U_F(r)$ potential. In left panel, the dotted green, dash-dotted magenta, short dashed cyan, and solid black lines represent the P_{el} ratios when the potential corresponding to each single channel is switched on at $V_0(r) + U_F(r)$ potential. In right panel, whereas, the dotted green, dash-dotted magenta, short dashed cyan, and solid black lines represent the P_{el} ratios when the potential corresponding to two channel coupling is switched on at $V_0(r) + U_F(r)$ potential.

the optical model potential. In this study, therefore, we will look at the contribution of each channel and see what the main contribution is. To this end, we will look at the change in elastic scattering cross-section by adding (or switching on) each channel to $V_0(r) + U_F(r)$ potential and investigate how much the contribution of each channel affects the rainbow peak. We also plan to look at contributions to pair channel (two channel coupling).

As shown in Fig. 3 (a), it can be easily observed that the suppression of P_{el} ratio due to the nuclear part of the breakup reaction potential (the solid black line) is the largest. This can also be confirmed in the values of the reaction cross-sections listed in Table III. Through this figure, however, it is not clear whether the contribution of a specific channel causes the rainbow peak to disappear. To clearly see the contribution of specific channels to the disappearance of the rainbow peak, so, we paired (or coupled) each channel with its Coulomb, nuclear, inelastic, and breakup reaction parts, respectively. As a result, we can obtain Fig. 3 (b). From Fig. 3 (b), we can carefully infer that the greatest contribution to the suppression of the rainbow peak is due to pairing of the nuclear part [switch on $U_{inel.}^N(r)$

+ $U_{\text{br}}^{\text{N}}(r)$; the dash-dotted magenta line]. It is also seen that the contribution of breakup reaction [switch on $W_{\text{br}}^{\text{C}}(r) + U_{\text{br}}^{\text{N}}(r)$; the solid black line] are larger than that of inelastic scattering [switch on $W_{\text{inel}}^{\text{C}}(r) + U_{\text{inel}}^{\text{N}}(r)$; the short dashed cyan line]. Finally, it can be seen that the contributions of Coulomb excitation interaction due to two low-lying E2 resonance states [switch on $W_{\text{inel}}^{\text{C}}(r) + U_{\text{br}}^{\text{C}}(r)$; the dotted green line] are relatively small. This means that we can once again confirm that this contribution is not the main one as mentioned above [16]. As a result, it can be interpreted that the ^{17}Ne projectile can be more easily excited or broken up by nuclear interaction than by the Coulomb one generated by the target nucleus.

B. CC calculations

So far, we have calculated the elastic, inelastic scattering, breakup reaction, and fusion cross-sections for $^{17}\text{Ne} + ^{208}\text{Pb}$ system using the OM. In the Ref. [16], the ^{15}O production cross section is calculated treating $\frac{5}{2}^-$ state [$E_x = 1.764$ MeV] as breakup channel using CC method. So, we try to calculate again for the same system using CC method [27] for comparison of analysis of Ref. [16] on our OM parameters. We endeavored to understand how the coupling effects of the potentials generated in the OM are reintergrated within the CC framework. When performing calculations for each coupling, the DPP potentials associated with each coupling were excluded from the calculated OM potential. Thus, we aimed to examine the effect of breakup using CC. Consequently, in Eq. (2) involving breakup effects, we replaced the breakup potential U_{br} with its counterpart calculated using the CC method.

First of all, we want to perform the CC calculations associated with set (A) of Table II which has no nuclear parts for inelastic, and the $\frac{5}{2}^-$ state [$E_x = 1.764$ MeV] and $\frac{3}{2}^-$ state [$E_x = 2.692$ MeV] are treated as the breakup interactions. In this calculation, $\frac{3}{2}^-$ state [$E_x = 2.692$ MeV] are added differently with Ref. [16]. For reference, the nuclear deformation length (δ_n) corresponding to the $\frac{5}{2}^-$ and $\frac{3}{2}^-$ states are used $\delta_1 = 2.14$ and $\delta_2 = 1.82$, respectively.

As a result, we plotted the theoretical P_{el} ratio and angular distribution of the breakup cross-section as the dashed blue line simultaneously using set (A) parameters in Fig. 4. Because the theoretical angular distribution of the breakup reaction cross-section is not very large, as shown in Fig. 4 (b), it can be seen that the theoretical P_{el} ratios do not

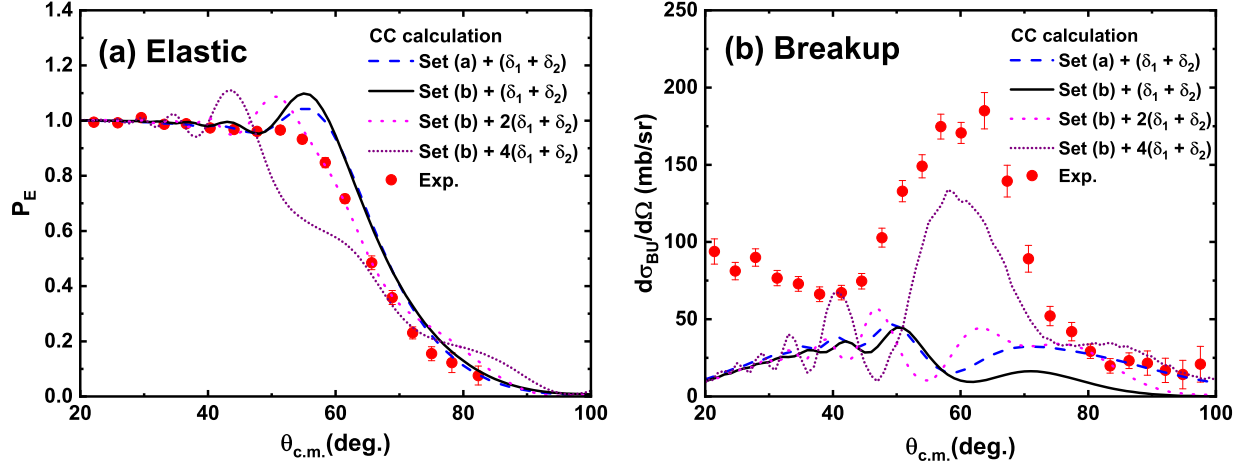


FIG. 4: Same as Fig. 2 but for CC calculations. The dashed blue and solid black lines represent the theoretical angular distribution of the breakup cross-sections obtained from CC calculations using the sets (A) and (B), and two nuclear deformation lengths $(\delta_1 + \delta_2)$ in Table II, respectively. On the other side, the dotted magenta and short-dotted violet lines represent those obtained from CC calculations using the set (B) and the double and quadruple of two nuclear deformation lengths, respectively.

suppresses sufficiently to satisfy the experimental P_{el} data.

In the same way, next, we perform the CC calculations associated with set (B) of Table II which is considered the additional coupling of the potentials of nuclear parts for inelastic and the $\frac{5}{2}^-$ state and $\frac{3}{2}^-$ state for the breakup interaction. The theoretical P_{el} ratio and angular distribution of the breakup cross-section are plotted as the solid black line in Fig. 4. As shown in Fig. 4 (b), however, it can be seen that the change in the theoretical P_{el} ratios is also insignificant because there is almost no change in breakup cross-section in this calculation compared to the calculation of set (A). This shows that the contribution of two low-lying states discussed above to breakup reaction, and additional channels as higher continuum states or transfer are need to describe for breakup cross section. In our OM calculations, so, we inserted a differential form of Woos-Saxon potential corresponding to the contributions of the nuclear part of the breakup reaction to consider additional states.

In the CC formalism, since it is difficult to consider all contributed channels to breakup reaction, we will simply adjust the nuclear deformation length mentioned above to see how the theoretical P_{el} ratios and angular distribution of the breakup cross-section change for testing the contribution of channels related to nuclear interaction. The contribution of

Coulomb interactions are presented around 40 degree, and show similar results with CC analysis of Ref. [16].

For simplicity, the theoretical P_{el} ratios and angular distribution of the breakup cross-section were examined by changing the nuclear deformation strength from two to four times. The results are plotted as the dotted magenta, short-dashed green, and short-dotted violet lines in Fig. 4. From this figure, it can be seen that as the nuclear deformation strength increases, the breakup reaction cross-section increases and gradually approaches the experimental data. This implies that the channels related to nuclear interaction, which are not concerned in this calculation, are important role to reproduce experimental data of P_{el} ratios and angular distribution of the breakup cross-section.

In conclusion, our CC calculations consider additional excited states [$\frac{3}{2}^-$ state ($E_x = 2.692$ MeV)] compared to the calculations performed in Ref. [16], but it is found that the additional excited states also could not explain the ^{15}O production cross section.

IV. CONCLUSIONS

In this study, we investigated the elastic scattering, inelastic scattering, breakup reaction, and fusion reaction of $^{17}\text{Ne} + ^{208}\text{Pb}$ system using OM and CC methods. Although only the experimental data of the elastic scattering and breakup cross-sections were available for $^{17}\text{Ne} + ^{208}\text{Pb}$ system, we successfully performed a simultaneous χ^2 analysis using the theoretical total fusion cross-section obtained from the coupled channel method.

Also, we investigate the contribution of each channel and see what the main contribution is. As a result, we can carefully infer that the greatest contribution to the suppression of the rainbow peak is due to paring of the nuclear part and the contributions of Coulomb excitation interaction due to two low-lying E2 resonance states are relatively small.

From the simultaneous χ^2 analysis of the $^{17}\text{Ne} + ^{208}\text{Pb}$ system, we can infer a strong suppression effect in the elastic scattering cross-section due to the nuclear interaction between the projectile and target nucleus, rather than the Coulomb interaction as observed in neutron-rich nuclei. The contribution of the direct reaction, comprising the inelastic scattering and breakup reaction cross-sections, accounted for almost half of the total reaction.

Finally, we perform the CC calculation using the parameters obtained from our OM calculation. Our CC calculations consider additional excited states [$\frac{3}{2}^-$ state ($E_x = 2.692$

MeV)] compared to the calculations performed in Ref. [16], but it is found that the additional excited states also could not explain the ^{15}O production cross section.

Acknowledgment

This work was supported by the National Research Foundation of Korea (Grant Nos. NRF-2021R1F1A1051935, NRF-2021R1F1A1046575, NRF-2020R1A2C3006177, NRF-2017R1E1A1A01074023 and NRF-2013M7A1A1075764) and by MSIT (No. 2018R1A5A1025563).

-
- [1] O. R. Kakuee, J. Rahighi, A. M. Sánchez-Benítez, M. V. Andrés, S. Cherubini, T. Davinson, W. Galster, J. Gómez-Camacho, A. M. Laird, M. Lamehi-Rachti, I. Martel, A. C. Shotter, W. B. Smith, J. Vervier, P. J. Woods, *Nucl. Phys. A* **728**, 339 (2003).
 - [2] A. M. Sánchez-Benítez, D. Escrig, M. A. G. Álvarez, M. V. Andrés, C. Angulo, M. J. G. Borge, J. Cabrera, S. Cherubini, P. Demaret, J. M. Espino, P. Figuera, M. Freer, J. E. García-Ramos, J. Gómez-Camacho, M. Gulino, O. R. Kakuee, I. Martel, C. Metelko, A. M. Moro, F. Pérez-Bernal, J. Rahighi, K. Rusek, D. Smirnov, O. Tengblad, P. Van Duppen, V. Ziman, *Nucl. Phys. A* **803**, 30 (2008).
 - [3] M. Cubero, J. P. Fernández-García, M. Rodríguez-Gallardo, L. Acosta, M. Alcorta, M. A. G. Alvarez, M. J. G. Borge, L. Buchmann, C. A. Diget, H. A. Falou, B. R. Fulton, H. O. U. Fynbo, D. Galaviz, J. Gómez-Camacho, R. Kanungo, J. A. Lay, M. Madurga, I. Martel, A. M. Moro, I. Mukha, T. Nilsson, A. M. Sánchez-Benítez, A. Shotter, O. Tengblad and P. Walden, *Phys. Rev. Lett.* **109**, 262701 (2012).
 - [4] V. Pesudo, M. J. G. Borge, A. M. Moro, J. A. Lay, E. Nácher, J. Gómez-Camacho, O. Tengblad, L. Acosta, M. Alcorta, M. A. G. Alvarez, C. Andreoiu, P. C. Bender, R. Braid, M. Cubero, A. Di Pietro, J. P. Fernández-García, P. Figuera, M. Fisichella, B. R. Fulton, A. B. Garnsworthy, G. Hackman, U. Hager, O. S. Kirsebom, K. Kuhn, M. Lattuada, G. Marquínez-Durán, I. Martel, D. Miller, M. Moukaddam, P. D. O'Malley, A. Perea, M. M. Rajabali, A. M. Sánchez-Benítez, F. Sarazin, V. Scuderi, C. E. Svensson, C. Unsworth and Z. M. Wang, *Phys. Rev. Lett.* **118**, 152502 (2017).

- [5] Y. Y. Yang, J. S. Wang, Q. Wang, D. Y. Pang, J. B. Ma, M. R. Huang, J. L. Han, P. Ma, S. L. Jin, Z. Bai, Q. Hu, L. Jin, J. B. Chen, N. Keeley, K. Rusek, R. Wada, S. Mukherjee, Z. Y. Sun, R. F. Chen, X. Y. Zhang, Z. G. Hu, X. H. Yuan, X. G. Cao, Z. G. Xu, S. W. Xu, C. Zhen, Z. Q. Chen, Z. Chen, S. Z. Chen, C. M. Du, L. M. Duan, F. Fu, B. X. Gou, J. Hu, J. J. He, X. G. Lei, S. L. Li, Y. Li, Q. Y. Lin, L. X. Liu, F. D. Shi, S. W. Tang, G. Xu, X. Xu, L. Y. Zhang, X. H. Zhang, W. Zhang, M. H. Zhao, Z. Y. Guo, Y. H. Zhang, H. S. Xu, and G. Q. Xiao, *Phys. Rev. C* **87**, 044613 (2013).
- [6] M. Romoli, E. Vardaci, M. Di Pietro, A. De Francesco, A. De Rosa, G. Inghima, M. La Commara, B. Martin, D. Pierroutsakou, M. Sandoli, M. Mazzocco, T. Glodariu, P. Scopel, C. Signorini, R. Bonetti, A. Guglielmetti, F. Soramel, L. Stroe, J. Greene, A. Heinz, D. Henderson, C. L. Jiang, E. F. Moore, R. C. Pardo, K. E. Rehm, A. Wuosmaa, and J. F. Liang, *Phys. Rev. C* **69**, 064614 (2004).
- [7] J. F. Liang, J. R. Beene, H. Esbensen, A. Galindo-Uribarri, J. Gomez del Campo, C. J. Gross, M. L. Halbert, P. E. Mueller, D. Shapira, D. W. Stracener, I. J. Thompson, and R. L. Varner, *Phys. Rev. C* **65**, 051603(R) (2002).
- [8] J. F. Liang, J. R. Beene, A. Galindo-Uribarri, J. Gomez del Campo, C. J. Gross, P. A. Hausladen, P. E. Mueller, D. Shapira, D. W. Stracener, R. L. Varner, J. D. Bierman, H. Esbensen, and Y. Larochelle, *Phys. Rev. C* **67**, 044603 (2003).
- [9] I. Tanihata, T. Kobayashi, O. Yamakawa, S. Shimoura, K. Ekuni, K. Sugimoto, N. Takahashi, T. Shimoda and H. Sato, *Phys. Lett. B* **206**, 592 (1988).
- [10] Meng Wang, G. Audi, F. G. Kondev, W. J. Huang, S. Naimi, and Xing Xu, *Chin. Phys. C* **41**, 030003 (2017).
- [11] A. Di Pietro, G. Randisi, V. Scuderi, L. Acosta, F. Amorini, M. J. G. Borge, P. Figuera, M. Fisichella, L. M. Fraile, J. Gomez-Camacho, H. Jeppesen, M. Lattuada, I. Martel, M. Milin, A. Musumarra, M. Papa, M. G. Pellegriti, F. Perez-Bernal, R. Raabe, F. Rizzo, D. Santonocito, G. Scalia, O. Tengblad, D. Torresi, A. Maira Vidal, D. Voulot, F. Wenander, and M. Zadro, *Phys. Rev. Lett.* **105**, 022701 (2010).
- [12] J. F. Liang, J. R. Beene, H. Esbensen, A. Galindo-Uribarri, J. Gomez del Campo, C. J. Grossa, M. L. Halbert, P. E. Mueller, D. Shapira, D. W. Stracener, and R. L. Varner, *Phys. Lett. B* **491**, 23 (2000).
- [13] Xue-ying He, Qin Dong, and Li Ou, *Chin. Phys. C* **44**, 054108 (2020).

- [14] Kyoungsu Heo, Myung-Ki Cheoun, Ki-Seok Choi, K. S. Kim, and W. Y. So, *Phys. Rev. C* **105**, 014601 (2022).
- [15] J. P. Fernández-García, M. Cubero, L. Acosta, M. Alcorta, M. A. G. Alvarez, M. J. G. Borge, L. Buchmann, C. A. Diget, H. A. Falou, B. Fulton, H. O. U. Fynbo, D. Galaviz, J. Gómez-Camacho, R. Kanungo, J. A. Lay, M. Madurga, I. Martel, A. M. Moro, I. Mukha, T. Nilsson, M. Rodríguez-Gallardo, A. M. Sánchez-Benítez, A. Shotter, O. Tengblad and P. Walden, *Phys. Rev. C* **92**, 044608 (2015).
- [16] J. D. Ovejas, I. Martel, D. Dell’Aquila, L. Acosta, J. L. Aguado, G. de Angelis, M. J. G. Borge, J. A. Briz, A. Chbihi, G. Colucci, C. Díaz-Martín, P. Figuera, D. Galaviz, C. García-Ramos, J. A. Gómez-Galán, C. A. Gonzales, N. Goyal, N. Keeley, K. W. Kemper, T. Kurtukian Nieto, D. J. Malenica, M. Mazzocco, D. Nurkić, A. K. Orduz, A. Ortiz, L. Palada, C. Parascandolo, A. Di Pietro, A. M. Rodriguez, K. Rusek, F. Salguero, A. M. Sánchez-Benítez, M. Sánchez-Raya, J. Sánchez-Segovia, N. Soić, F. Soramel, M. Stanoiu, O. Tengblad, N. Vukman, and M. Xarepe, *Phys. Lett. B* **843**, 138007 (2023).
- [17] M. J. Chromik, P. G. Thirolf, M. Thoennessen, B. A. Brown, T. Davinson, D. Gassmann, P. Heckman, J. Prisciandaro, P. Reiter, E. Tryggestad, and P. J. Woods, *Phys. Rev. C* **66**, 024313 (2002).
- [18] J. Marganec, F. Wamers, F. Aksouh, Yu. Aksyutina, H. Álvarez-Pol, T. Aumann, S. Beceiro-Novo, C. A. Bertulani, K. Boretzky, M. J. G. Borge, M. Chartier, A. Chatillon, L. V. Chulkov, D. Cortina-Gil, H. Emling, O. Ershova, L. M. Fraile, H. O. U. Fynbo, D. Galaviz, H. Geissel, M. Heil, D. H. H. Hoffmann, J. Hoffmann, H. T. Johansson, B. Jonson, C. Karagiannis, O. A. Kiselev, J. V. Kratz, R. Kulesa, N. Kurz, C. Langer, M. Lantz, T. Le Bleis, R. Lemmon, Yu. A. Litvinov, K. Mahata, C. Müntz, T. Nilsson, C. Nociforo, G. Nyman, W. Ott, V. Panin, S. Paschalis, A. Perea, R. Plag, R. Reifarh, A. Richter, C. Rodriguez-Tajes, D. Rossi, K. Riisager, D. Savran, G. Schrieder, H. Simon, J. Stroth, K. Sümmerer, O. Tengblad, S. Typel, H. Weick, M. Wiescher, and C. Wimmer, *Phys. Lett. B* **843**, 138007 (2023).
- [19] C. Mahaux, H. Ngo, and G. Satchler, *Nucl. Phys. A* **449**, 354 (1986).
- [20] B. T. Kim, W. Y. So, S. W. Hong, and T. Udagawa, *Phys. Rev. C* **65**, 044616 (2002).
- [21] W. Y. So, S. W. Hong, B. T. Kim, and T. Udagawa, *Phys. Rev. C* **69**, 064606 (2004).
- [22] L. C. Chamon, B. V. Carlson, L. R. Gasques, D. Pereira, C. De Conti, M. A. G. Alvarez, M. S. Hussein, M. A. Cândido Ribeiro, E. S. Rossi, Jr., and C. P. Silva, *Phys. Rev. C* **66**, 014610

(2002). references:

- [23] R. O. Akyuz and A. Winther, Proc. Enrico Fermi Int. School of Physics, 1979, 'Nuclear structure and heavy-ion reactions', ed. R.A. Broglia, C.H. Dasso and R. Ricci (North-Holland, Amsterdam, 1981) p. 491
- [24] W. G. Love, T. Terasawa, and G. R. Satchler, Nucl. Phys. A **291**, 183 (1977).
- [25] M. Andrés, J. Gómez-Camacho and M. Nagarajan, Nucl. Phys. A **579**, 273 (1994).
- [26] K. E. Rehm, W. Henning, J. R. Erskine, D. G. Kovar, M. H. Macfarlane, S. C. Pieper, and M. Rhoades-Brown, Phys. Rev. C **25**, 1915 (1982).
- [27] K. Hagino, N. Rowley, and A. T. Kruppa, Comput. Phys. Comm **123**, 143 (1999).
- [28] T. Udagawa and T. Tamura, Phys. Rev. C **29**, 1922 (1984).
- [29] M. S. Hussein, Phys. Rev. C **30**, 1962 (1984).